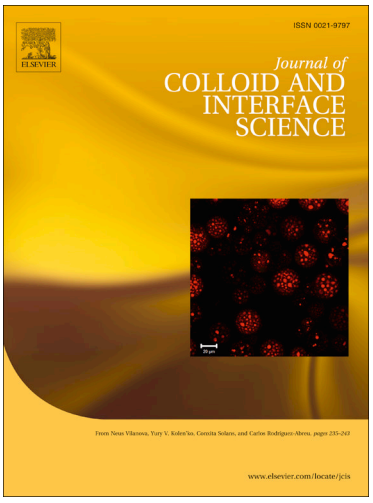


# iRGD-decorated red shift emissive carbon nanodots for tumor targeting fluorescence imaging

Yuanyuan Yang, Xuefeng Wang, Guochao Liao, Xiqiang Liu, Qiling Chen, Hongmei Li, Ling Lu, Peng Zhao, Zhiqiang Yu

PII: S0021-9797(17)31038-X
DOI: http://dx.doi.org/10.1016/j.jcis.2017.09.007
Reference: YJCIS 22758

To appear in: *Journal of Colloid and Interface Science*

Received Date: 31 July 2017
Revised Date: 5 September 2017
Accepted Date: 5 September 2017

Please cite this article as: Y. Yang, X. Wang, G. Liao, X. Liu, Q. Chen, H. Li, L. Lu, P. Zhao, Z. Yu, iRGD-decorated red shift emissive carbon nanodots for tumor targeting fluorescence imaging, *Journal of Colloid and Interface Science* (2017), doi: http://dx.doi.org/10.1016/j.jcis.2017.09.007

# iRGD-decorated red shift emissive carbon nanodots for tumor targeting fluorescence imaging

Yuanyuan Yang[a], Xuefeng Wang[b], Guochao Liao[c], Xiqiang Liu[d], Qiling Chen[a], Hongmei Li[a], Ling Lu[a], Peng Zhao[a,*], Zhiqiang Yu[a,*]

[a]*Guangdong Provincial Key Laboratory of New Drug Screening, School of Pharmaceutical Sciences, Southern Medical University, Guangzhou 510515, P. R. China.*

[b]*Department of Obstetrics and Gynecology, Zhujiang Hospital, Southern Medical University, Guangzhou 510282, P. R. China.*

[c]*International Institute for Translational Chinese Medicine, Guangzhou University of Chinese Medicine, Guangzhou, Guangdong 510006, P. R. China.*

[d]*Guangdong Provincial Key Laboratory of Stomatology, Department of Oral and Maxillofacial Surgery, Guanghua School and Hospital of Stomatology, Sun Yat-Sen University, Guangzhou, 510055, P. R. China.*

*Corresponding author.

E-mail addresses: smuzp@smu.edu.cn

yuzq@smu.edu.cn

**Graphical abstract**

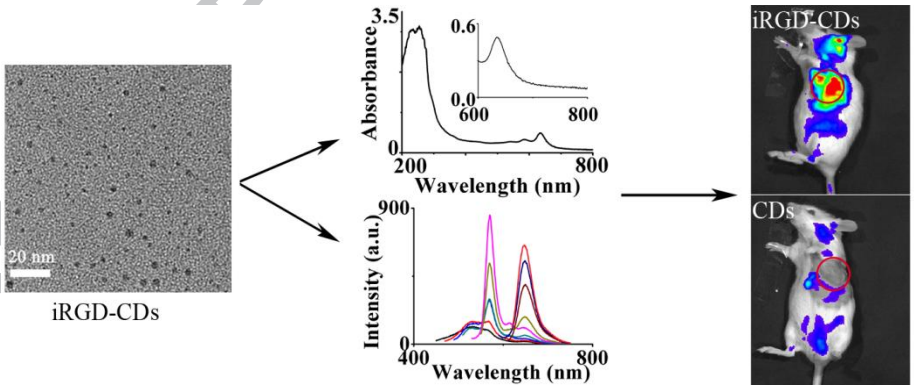

**Abstract:** Carbon nanodots (CDs) have been exhibiting increasing applications owing to their luminescence properties and biocompatibility as imaging probes in diagnosis. However, poor tumor targeting and penetration of CDs is still the biggest challenge limiting their tumor imaging efficacy. To improve the tumor targeting and penetration efficiency of CDs, we developed an active tumor targeting imaging system by simply fabricating a tumor-homing penetration peptide iRGD (CRGDKGPDC) to red shift emissive CDs (iRGD-CDs) with a physical method. Particularly, iRGD-CDs showed a small size and red shift fluorescence signals as CDs, which made iRGD-CDs suitable for *in vivo* fluorescence imaging. iRGD-CDs showed higher cellular uptake *in vitro*, while presented higher penetration and accumulation in tumor tissue *in vivo*, leading to better tumor imaging efficacy. In conclusion, decoration with iRGD could significantly increase the permeability of CDs in tumor vessels and tumor tissue, generating more CDs leaking out from tumor vasculature, consequently improving the sensitivity of tumor imaging.

**Keywords:** Carbon nanodots; iRGD; tumor targeting; fluorescence imaging; deep penetration

## 1. Introduction

In recent years, carbon-based nanomaterials, including graphene quantum dots, polymer dots, carbon nanotubes, fullerene, nanodiamonds and carbon nanodots (CDs) have been extensively applied in many fields [1-7]. Among them, CDs, the new class of nanomaterials have received considerable attention owing to their intrinsic advantages, including photoluminescence, good water solubility, good biocompatibility, ease of functionalization, low toxicity, low immunogenicity, and resistance to photobleaching [8-14]. Nowadays, CDs hold great potential in sensing, fluorescence imaging, photoacoustic imaging, magnetic resonance imaging, photothermal treatment and drug delivery, which is considered to be a potential eco-friendly alternative to semiconductor quantum dots [15-24]. However, the luminescence of most CDs is still with short excitation and emission wavelengths, which is not suitable for *in vivo* imaging because of high background signal and poor tissue penetration. In the past several years, more and more CDs with red shift luminescence were prepared to reduce the background signal as well as increase tissue penetration, which can be more adapted in *in vivo* fluorescence imaging [25-28]. However, CDs can only passively accumulate in tumor via the enhanced permeability and retention (EPR) effect, which is not sufficient for tumor targeting of CDs [29-32]. Therefore, it is important to develop novel CDs equipped with both red shift fluorescence and active tumor targeting capacity. To

improve the tumor targeting and penetration of nanomaterials, various targeting strategies and ligands have been applied to direct them to tumors [33-37]. Among tumor targeting moieties, peptides have been utilized in cancer diagnostics and therapeutics due to their advantages such as low toxicity, low immunogenicity, fast clearance, high specificity, and high versatility [38-40]. As a tumor-homing penetration peptide, iRGD, firstly homes to tumors by initially targeting $\alpha_v\beta_3$ integrin receptors, which are specifically expressed in the tumor vasculature and tumor cells. Then it binds to neuropilin-1 (NRP-1), consequently triggering tissue penetration [30, 41-45]. Physically decoration with iRGD or chemically conjugated to iRGD can not only improve tumor penetration of various compositions but also specifically enhanced vascular and tissue permeability in a tumor-specific and NRP-1- dependent manner [46-49]. In this study, we developed an active tumor targeting imaging system only through physically decorating iRGD onto a red shift emissive CDs (iRGD-CDs). Then the luminescence properties, particle size, surface groups, serum stability and hemcompatibility of iRGD-CDs were carefully evaluated. Cellular uptake and cell toxicity were tested on $\alpha_v\beta_3$ and NRP-1 receptors overexpressed 4T1 cells *in vitro* [50, 51], and an appropriate control cell experiment was carried out using A2780 cells with low $\alpha_v\beta_3$ [52]. *In vivo* tumor imaging and tissue distribution studies were carried out to elucidate the tumor targeting effect of iRGD-CDs.

## 2. Materials and methods

### *2.1. Materials*

Melanin (99%) was purchased from Alfa Aesar (Ward Hill, USA). 3-(4, 5-dimethylthiazol-2-yl)-2, 5-diphenyltetrazolium bromide (MTT) and 4′,6-diamidino-2-phenylindole (DAPI) was purchased from Beyotime Institute Biotechnology (Haimen, China). Rabbit anti-CD34 polyclonal antibody was obtained from eBioscience, Inc., (San Diego, USA). Rabbit neuropilin-1 polyclonal antibody (NRP-1) was purchased from 4A Biotech Co., Ltd. (Beijing, China). Rabbit anti-integrin beta-3 was obtained from Abcam Ltd. (Hong Kong, China). Cy3-conjugated donkey anti-rabbit secondary antibody and Cy3-conjugated donkey anti-rat secondary antibody were purchased from Jackson Immuno Research Laboratories, Inc. (West Grove, USA). Plastic cell culture dishes and plates were obtained from Wuxi NEST Biotechnology Co. Ltd (Wuxi, China). Dulbecco's Modified Eagle Medium cell culture medium (DMEM) containing 10% of fetal bovine serum (FBS), 100 U $mL^{-1}$ of penicillin G and 100 U $mL^{-1}$ of streptomycin sulfate were obtained from

Life Technologies (Grand Island, USA). 4T1 cell line and A2780 cell line were obtained from the Institute of Biochemistry and Cell Biology, Shanghai Institutes for Biological Sciences, Chinese Academy of Sciences (Shanghai, China). Female BALB/c mice (20 ± 2 g) were purchased from Laboratory Animal Centre of Southern Medical University (Guangzhou, China) and were maintained under standard housing conditions. All animal experiments were performed under the guidelines evaluated and approved by the ethics committee of Southern Medical University, China.

*2.2. Preparation and characterization*

iRGD-CDs were prepared by adsorbing iRGD onto CDs obtained from previous study [53]. Briefly, 1.0 g of water-soluble melanin was dissolved in 6 mL of deionized water and the reaction mixture was heated at 220$^{o}$C for 48 h. After cooled to room temperature, the solution was filtered (pore size 0.45 μm) and then iRGD at the concentration of 3.8 mg/ml was added into the above-mentioned CDs solution. Morphology of iRGD-CDs was captured by transmission electronic microscopy (TEM) (JEM-2100F, Japan). Ultraviolet-visible (UV-vis) spectra of iRGD-CDs and CDs in water were recorded using a Varian cary 100 conc UV-vis spectrophotometer (Varian, USA). Fluorescence spectra of iRGD-CDs and CDs were recorded using a Shimadzu RF-5301PC spectrofluorophotometer (Shimadzu, Japan). Fourier transform infrared (FT-IR) spectra of iRGD-CDs and CDs in KBr was collected by using a Nexus 670 (Thermo Nicolet, USA).

*2.3. Stability and hemocompatibility*

The serum stabilities of iRGD-CDs and CDs were investigated in PBS with different concentrations of FBS. iRGD-CDs and CDs were suspended in 0%, 10% or 50% FBS and incubated in a shaker (37$^{o}$C, 100 rpm/min). The absorption of iRGD-CDs and CDs at 490 nm was detected by a microplate reader (Multiskan MK3, Thermo, USA) at 0, 1, 2, 4, 6, 8, 10, 12 and 24 h. In addition, fluorescence spectra of iRGD-CDs incubated with 10% FBS was recorded at 0, 2, 4, 12 and 24 h.

Whole blood was collected from BALB/c mice using heparin as the anticoagulant. After centrifugation at 2500 rpm for 5 min, the red blood cells were resuspended in PBS (pH=7.4) to get 2% erythrocyte stock dispersion (ESD). Different concentrations of iRGD-CDs and CDs were added into 2% ESD and incubated at 37$^{o}$C for different time. The absorption at 490 nm was

detected by a microplate reader (Thermo Scientific Varioskan Flash, USA). 1% of Triton X-100 was used as positive control while PBS (pH=7.4) was used as negative control.

*2.4. Cytotoxicity*

MTT assay was used to investigate the cytotoxicity of iRGD-CDs and CDs. 4T1 cells were seeded into the 96-well plates at a density of 1 x $10^5$ per well. After 24 h incubation, iRGD-CDs and CDs were added into each well with final concentrations from 128 μg/mL to 1 μg/mL. After another 24 h incubation, 10 μL MTT solution (5 mg/mL) was added into each well and incubated for 4 h, then the medium was replaced by 150 μL dimethyl sulfoxide and the absorbance was measured by a microplate reader (Thermo Scientific Varioskan Flash, USA) at 490 nm.

*2.5. Cellular uptake*

4T1 cells of logarithmic growth phase were inoculated in 12-well plates at a density of 1 × $10^5$ cells per well. After incubation for 24 h, iRGD-CDs and CDs were added to the plates, respectively, with the same dose of 150 μg/mL. After incubation for 1, 2, 4 h, the cells were harvested. A flow cytometer (Beckman Coulter, USA) was used to measure the fluorescence intensity of two groups.

For qualitative experiments, 4T1 cells were plated on a 12 mm coverslips in 6-well plates at a density of 1 × $10^5$ cells per well and incubated at 37°C for 24 h. The 4T1 cells were treated with iRGD-CDs and CDs for 1, 2, 4 h at an equivalent concentration of 150 μg/mL and with a final concentration of 600 μg/mL, 125 μg/mL and 37.5 μg/mL for 2 h. After the cells were washed and fixed at room temperature, DAPI (0.5 μg/mL) was added to stain the nuclei, then the coverslips were placed on the slides for fluorescent imaging by a confocal microscope (A1+, Nikon, Japan).

To confirm the *in vitro* specific binding efficiency of iRGD-CDs against $\alpha_v\beta_3$ integrin, we conducted a competition assays on A2780 cells with low $\alpha_v\beta_3$ by a confocal microscope. A2780 cells were treated consistent with 4T1 cells except treating with iRGD-CDs and CDs for 1, 2, 4 h at an equivalent concentration of 150 μg/mL.

*2.6. In vivo and ex vivo imaging*

Tumor-bearing mice were established by injecting 4T1 cells into the left upper thigh subcutaneous region of mice with a density of 5 × $10^6$ cells in 0.1 mL of PBS. After 10 days implantation, tumors established (about 100 $mm^3$) and the mice were intravenously administrated with iRGD-CDs and control CDs at the same dose of 66.3 mg/kg via tail vein injection. Then the

fluorescence distribution of whole body was acquired at different time using an *in vivo* imaging system (IVIS Lumina, Caliper, U.S.A.). After the mice sacrificed, their tumors and normal tissues were collected and subjected to *ex vivo* fluorescence imaging as well. *In vivo* fluorescence imaging conditions: IVIS Lumina III Imaging System was used to perform optical imaging studies. The scanning parameters included as follows: excitation wavelength: 560 nm, emission wavelength: 620 nm, field of view: 12.5 cm and fluency rate: 2 $mW/cm^2$. The camera was set to maximum gain, a binning factor of 4, and a luminescent exposure time of 0.5 s.

*2.7. In Vivo Tumor and Tissue Distribution*

The isolated tumors and major tissues of mice obtained in section 2.6 were collected and first fixed with 4% (w/v) paraformaldehyde for immunofluorescence study. After overnight dehydrating with 15% (w/v) sucrose followed by extra 30% (w/v) sucrose for another 24 h, all of these tumors and tissues were prepared with a thickness of 10 μm thickness using a freezing microtome (Leica, Germany). Cell nuclei staining were performed with DAPI (0.5 μg/mL), tumor vasculature was stained by rat anti-mouse CD34 antibody and Cy3-labled donkey anti-rat secondary antibody, NRP-1 was stained by rabbit anti-mouse NRP-1 antibody and Cy3-labeled donkey anti-rabbit secondary antibody, and $\alpha_v\beta_3$ was stained by rabbit anti-mouse $\alpha_v\beta_3$ antibody and Cy3-labeled donkey anti-rabbit secondary antibody. Then, the images were captured using confocal microscopy (A1+, Nikon, Japan). The quantified results were analyzed using the ImageJ software package.

*2.8. Statistical Analysis.*

Statistical differences between experimental and control groups was analyzed by T Test (IBM SPSS 22.0), $p < 0.05$, 0.01, and 0.001 were considered to be a statistically significant difference and remarked with *, **, ***, respectively.

**3. Results and discussion**

*3.1. Preparation and characterization*

First, iRGD-CDs were synthesized only via physically fabricating iRGD to CDs. According to the TEM and the analysis results (Figure 1A), iRGD-CDs had a uniform diameter of 3.3 ± 0.57 nm. High-resolution TEM images illustrate that most iRGD-CDs have well-resolved lattice structures with a *d* spacing value of 0.22 nm (Figure 1B, C). The UV-vis spectra of iRGD-CDs showed two ranges of broad absorptions located at 200 nm to 400 nm and 500 nm to 700 nm (Figure 1D)

correspondingly with a wide excitation range from 440 nm to 615 nm with two maximum emissions at 570 nm and 645 nm (Figure 1E), which was consistent with previous published CDs study (Figure 1F, G). According to the fluorescence spectra, the longer excitation and emission renders iRGD-CDs also suitable for *in vivo* fluorescence imaging because of the deeper tissue penetration depth with reduced background consistent with CDs. Fourier transform infrared (FT-IR) spectra was performed to further characterize iRGD-CDs. In the FT-IR analysis of iRGD-CDs (Figure S1A), the following vibrations were observed: stretching vibration of C-OH at 3405.67 $cm^{-1}$, stretching vibration of N-H at 3139.54 $cm^{-1}$, asymmetric stretching vibrations of C−NH−C at 1170.58 $cm^{-1}$, stretching vibrations of C=C at 1625.7, 1529.27, and 1402 $cm^{-1}$ and stretching vibration of =CH at 3004.55 $cm^{-1}$, indicating that the structures of iRGD-CDs might contain polycyclic aromatic and aromatic CN groups [12], which was consistent with CDs (Figure S1B).

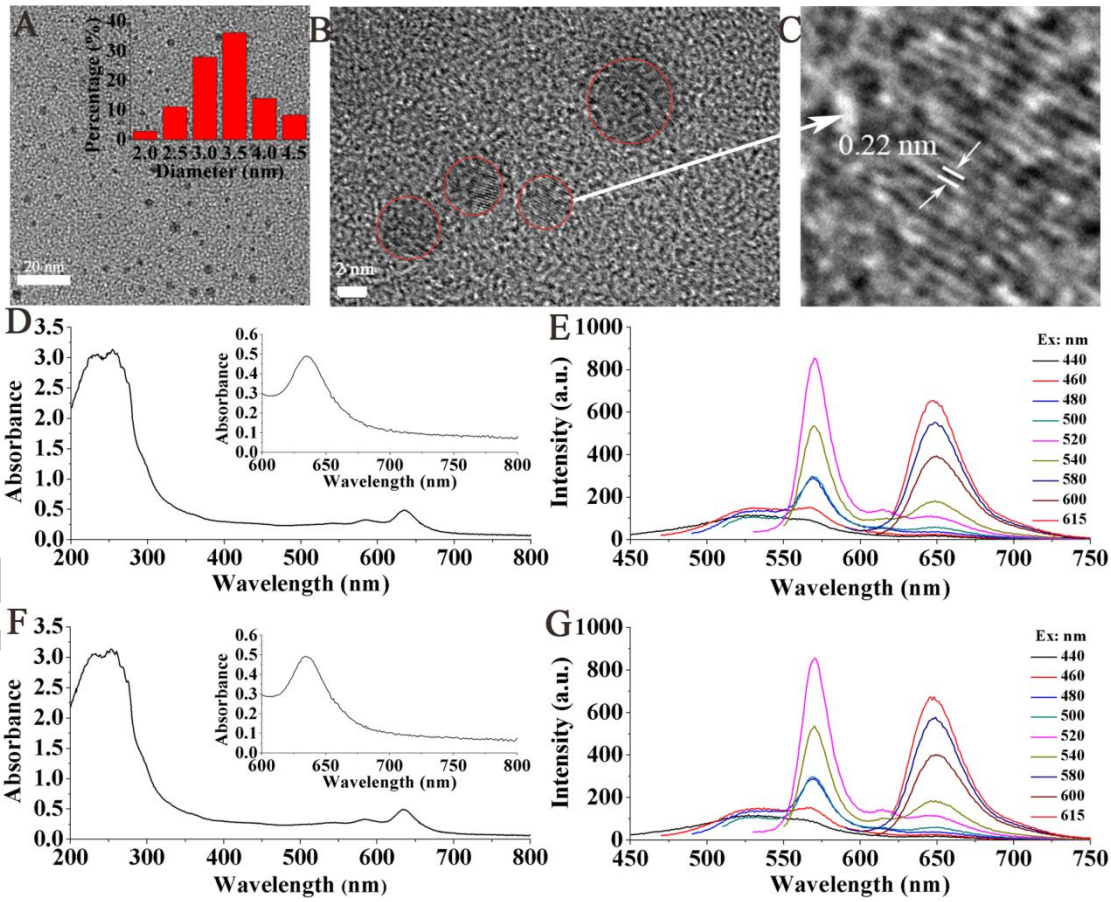


**Figure 1.** Characterization of iRGD-CDs and CDs. (A) TEM image of iRGD-CDs, bar represents 20 nm. The inset image is the diameter distribution of iRGD-CDs. (B) High-resolution TEM image of iRGD-CDs, bar represents 2 nm. (C) Highlighted area of B. (D) The absorbance spectra

of iRGD-CDs. The inset showed enlarged absorbance spectra of the iRGD-CDs from 600 to 800 nm. (E) Fluorescent spectra of iRGD-CDs. (F) The absorbance spectra of CDs. The inset showed enlarged absorbance spectra of the CDs from 600 to 800 nm. (G) Fluorescent spectra of CDs.

*3.2. Stability*

For *in vivo* application, protein adsorption formed on the surface of nanoparticles is one of the major concerns that altered stability and *in vivo* behavior of nanoparticles [54]. After incubation with FBS, the absorptions of iRGD-CDs and CDs at 490 nm increased gradually, which was positively related to the incubation time and the concentration of FBS (Figure 2A), suggesting that iRGD-CDs and CDs could contact with serum protein and lead to protein adsorption. This important issue needed to be further evaluated. However, with prolonged incubation time, the fluorescence intensity of iRGD-CDs did not decrease dramatically (Figure S2), which would have positive contributions towards applications in fluorescence imaging *in vivo*.

Hemocompatibility is another concern for *in vivo* fluorescence imaging application because poor hemocompatibility of nanoparticles could lead to acute toxicity to body. Despite increasing the concentration of iRGD-CDs and CDs promoted the hemolysis rate, the hemolysis rates in two groups at different concentrations were all lower than 6% after 8 h incubation (Figure 2B, C), suggesting that iRGD-CDs and CDs had low hemolysis potential, which was suitable for *in vivo* application.

*3.3. Cytotoxicity*

For *in vivo* application, the toxicity of iRGD-CDs to cells was another issue should be considered. To demonstrate the toxicity of iRGD-CDs to cells, 4T1 cells were incubated with a series of different concentrations of iRGD-CDs for 24 h. The cell viability presented no obvious change between control and iRGD-CDs treated cells for 24 h at the concentrations as high as 64 μg/mL (Figure 2D), suggesting iRGD-CDs have relatively low cytotoxicity consistent with CDs. Further elevating the iRGD-CDs concentration to 128 μg/mL could inhibit the 4T1 cell growth. This suppression of cell growth may be due to the positive zeta potential in low pH value, thus resulting in more CDs accumulated in the nuclei, which is consistent with other CDs study [53]. However, the toxicity of CDs could be reduced after surface modification, such as PEGylation [12], which needs further evaluations.

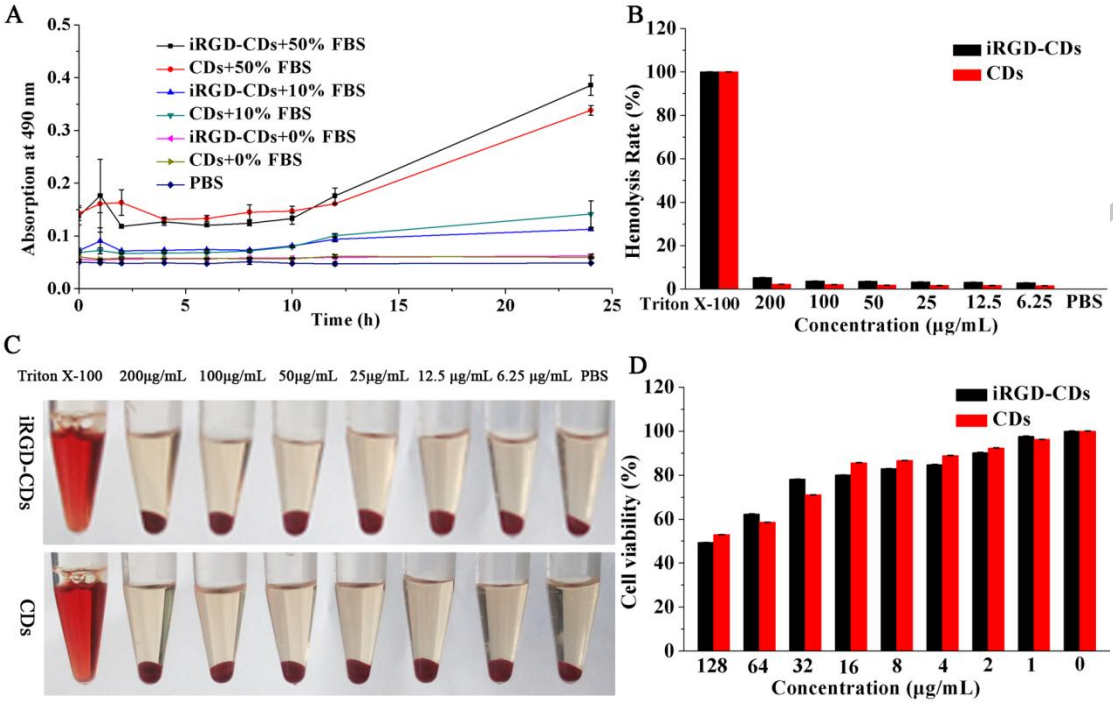


**Figure 2.** (A) Stability of iRGD-CDs and CDs in different concentration of FBS. (B, C) Hemolysis rate (B) and image (C) of 2% red blood cells after incubation with different concentration of iRGD-CDs and CDs for 8 h. (D) Cytotoxicity of iRGD-CDs and CDs to 4T1 cells after 24 h incubation. (n = 6).

*3.4. Cellular uptake*

In order to determine the homing and cell penetration ability of iRGD-CDs, the cellular uptake of the iRGD-CDs by 4T1 cells was investigated using a confocal laser scanning microscope and flow cytometry. Confocal laser microscopy images showed that the fluorescence intensity of 4T1 cells incubated with iRGD-CDs was much stronger than that of CDs groups at different concentration (Figure 3A). On the other aspect, obvious differences of cellular uptake between iRGD-CDs group and CDs group after incubation for 1, 2 and 4 h at an equivalent concentration of 150μg/mL (Figure 3B) were also obtained. Both stronger fluorescence intensity and cellular uptake differences demonstrated that iRGD-CDs could significantly improve the tumor targeting and sensitivity of CDs. These results were further determined by flow cytometer analysis. The fluorescence intensity between the iRGD-CDs group and the CDs group presented apparent difference at 1, 2 and 4 h (Figure 3C), which also suggested that iRGD could specifically recognize the highly expressed NRP-1 and $\alpha_v\beta_3$ integrin receptors on 4T1 cells, thus facilitating the internalization and tumor imaging sensitivity of CDs [55]. To prevent non-specific binding of

iRGD-CDs, an appropriate cells control experiment was tested on A2780 cells with low $\alpha_v\beta_3$. The fluorescence intensity between the iRGD-CDs group and the CDs group on A2780 cells presented no difference at different concentration of 37.5, 150, 600 μg/mL after incubation for 2 h (Figure S3), indicating that iRGD-CDs showed lower binding in the $\alpha_v\beta_3$-negative A2780 cells.

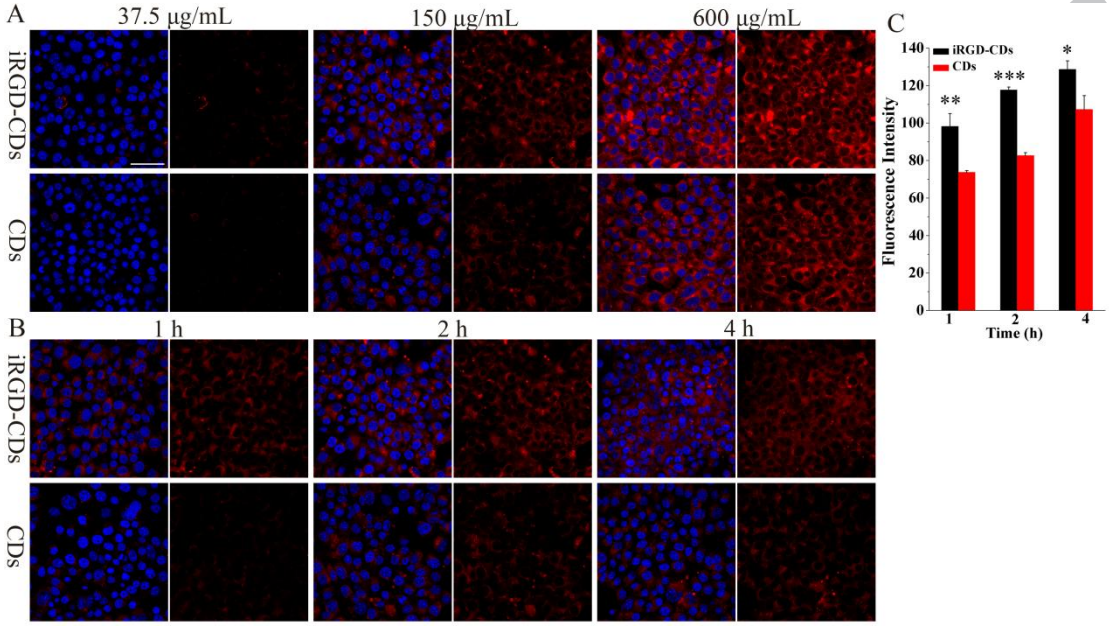


**Figure 3.** Cellular uptake. Confocal images of cellular uptake on 4T1 cells after being treated with iRGD-CDs and CDs. (A) indicates the treatment at different concentrations of 37.5, 150, 600 μg/mL after incubation for 2 h. (B) indicates the treatment at an equivalent concentration of 150 μg/mL after different incubation for 1, 2 and 4 h. Blue indicated nuclei, red indicated CDs and bar represents 50 μm. (C) Cellular uptake of two groups on 4T1 cells measured by flow cytometer. *, $p< 0.05$, **, $p< 0.01$, ***, $p< 0.001$, among the marked group and CDs group.

*3.5. In vivo and ex vivo imaging*

To validate the tumor targeting ability of iRGD-CDs, *in vivo* and *ex vivo* imaging of 4T1 tumor-bearing mice was conducted using an *in vivo* imaging system (IVIS Spectrum, Caliper, USA). After 4 h injection, whole body images showed no difference between the iRGD-CDs group and CDs group, while the iRGD-CDs group showed much higher accumulation efficiency and displayed much stronger fluorescent intensity in tumor compared to CDs group both at 12 h and 24 h (Figure 4A). This was also supplemented by semi-quantitative data obtained from tumors (Figure 4C), indicating that iRGD-CDs could be efficiently delivered to 4T1 tumor tissue. In addition, the distribution of tumor and normal tissue showed that the fluorescent intensity of tumor marked with iRGD-CDs group was much higher than that of CDs group (Figure 4B), which was

consistent with the quantitative distribution measure of 4T1 tumor (Figure 4D). The iRGD-CDs and CDs showed lower distribution in normal tissues after 24 h, probably owing to fast clearance depended on small size [1, 56]. Due to overexpression of NRP-1 and $\alpha_v\beta_3$, iRGD-CDs increased the penetration of CDs from tumor vasculature and tumor tissue, which confirmed that iRGD-CDs could home to 4T1 tumor sites selectively and noticeably enhance accumulation of CDs in 4T1 tumor in favor of tumor imaging [57, 58].

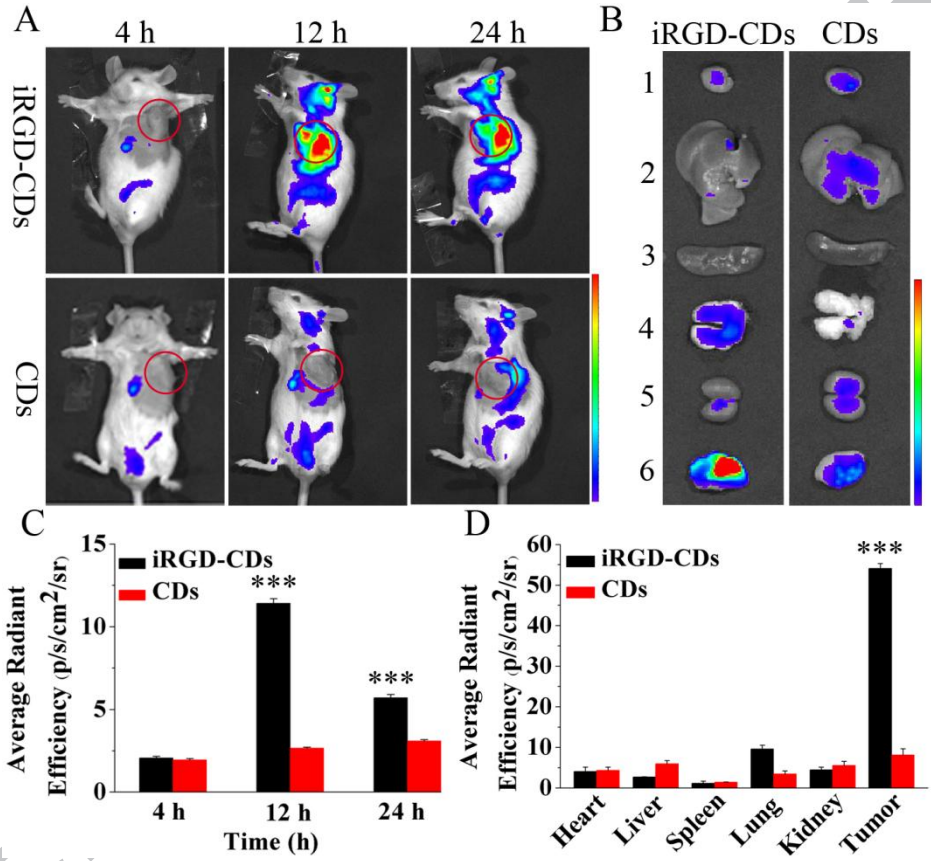


**Figure 4.** *In vivo* distribution of iRGD-CDs and CDs in 4T1-bearing mice. (A) Living imaging of BALB/c mice after intravenous injection with iRGD-CDs and control CDs; bar indicates average radiant efficiency from $4.5 \times 10^8$ to $1.8 \times 10^9$. (B) *Ex vivo* imaging of tumor and normal tissue after 24 h injection. 1 indicates Heart, 2 indicates Liver, 3 indicates Spleen, 4 indicates Lung, 5 indicates Kidney, 6 indicates Tumor; bar indicates average radiant efficiency from $1.0 \times 10^8$ to $1.0 \times 10^9$. (C) Semi-quantitative data of signal in tumor sites in living mice. (D) Semi-quantitative data of signal in tumors and organs. ***, $P < 0.001$, among the marked group and CDs group.

*3.6. In Vivo Tumor and Tissue Distribution*

Tumor slices were stained with anti-$\alpha_v\beta_3$, anti-NRP-1 and anti-CD34 antibody to further elucidate the target effect of iRGD-CDs. The fluorescence intensity of iRGD-CDs group was much higher

than that of CDs group (Figure 5), which was believed to be due to iRGD peptide could increase tumor vascular and tissue permeability in a $\alpha_v\beta_3$ and NRP-1 dependent 4T1 tumor, leading more CDs being spilled from the vessels, thus deep tumor penetration was obtained [59]. The tumor penetration ability was evaluated with tumor neovessels stained by anti-CD34 antibody. Attributed to enhanced access to the extravasculature, more iRGD-CDs could reach the deep tumor which was far away from the neovessels (Figure 5C). Furthermore, obviously more internalization was found in the iRGD-CDs group than in the CDs group since the tumor cell penetration enhanced by iRGD peptide. Moreover, the distribution of two groups was also evaluated in normal tissues (Figure S4). The iRGD-CDs group showed lower distribution in other normal tissue than tumor, illustrating the relatively reduced toxicity. These results all indicated that decoration with iRGD peptide could improve the tumor targeting efficiency of CDs.

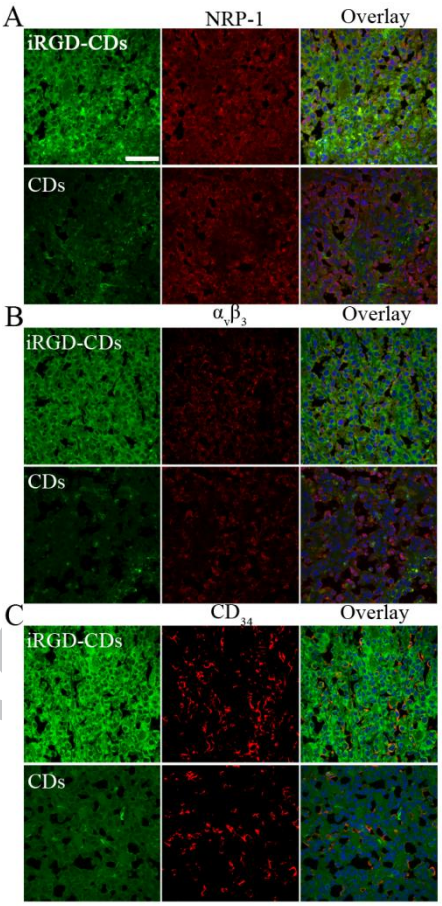


**Figure 5.** Fluorescence distributions of iRGD-CDs and CDs in 4T1 tumors at 24 h. Tumor tissues were stained with anti-NRP-1 (A), anti-$\alpha_v\beta_3$ (B), and anti-CD34 antibodies (C), bar represents 50 μm.

**4. Conclusions**

In this study, we developed an active tumor targeting imaging system with simple physical synthesis by fabricating iRGD to red shift emissive CDs (iRGD-CDs). iRGD-CDs had red shift fluorescence consistent with CDs, enabling iRGD-CDs utilized for *in vivo* fluorescence imaging. Well serum stability and low hemolysis rate of iRGD-CDs contributed great potential for *in vivo* imaging application. *In vitro* cellular study suggested that iRGD-CDs showed an enhanced accumulation in the 4T1 cells, leading to an excellent tumor cell imaging. Based on the control results, iRGD-CDs could specifically recognize the highly expressed $\alpha_v\beta_3$ integrin receptors on 4T1 cells instead of non-specific binding. *In vivo* fluorescence imaging demonstrated that iRGD-CDs could selectively accumulate in the tumor site, increasing the capacity to diagnosis the tumor, which provided significant advances of tumor imaging compared to previous negative targeting CDs [25, 26]. More importantly, this enhancement is really simple, compact and biocompatible, without chemically conjugating CDs to iRGD peptide. Thus, iRGD-CDs displayed better tumor imaging effect, and it may act as a promising agent in tumor diagnosis in the future.

**Acknowledgements**

The work was granted by National Natural Science Foundation of China (21605077, 81541086，81372885), the Science and Technology Planning Program of Guangzhou City, China (Grant nos. 201707010467), the Educational Commission of Guangdong Province, China (Grant Nos. 2016KZDXM031) and the Major Special Research Collaborative Innovation of Guangzhou (201604020160).

**References**

[1] L. Cao, M.J. Meziani, S. Sahu, Y.P. Sun, Accounts of Chemical Research 46 (2013) 171.

[2] W. Li, Z. Zhang, B. Kong, S. Feng, J. Wang, L. Wang, J. Yang, F. Zhang, P. Wu, D. Zhao, Angewandte Chemie 52 (2013) 8151.

[3] L.P. McGuinness, Y. Yan, A. Stacey, D.A. Simpson, L.T. Hall, D. Maclaurin, S. Prawer, P. Mulvaney, J. Wrachtrup, F. Caruso, R.E. Scholten, L.C. Hollenberg, Nature Nanotechnology 6 (2011) 358.

[4] A. Antonucci, J. Kupis-Rozmyslowicz, A.A. Boghossian, ACS Applied Materials & Interfaces 9 (2017) 11321.

[5] Q. Xu, T. Kuang, Y. Liu, L. Cai, X. Peng, P. Zhao, Z. Yu, N. Li, Journal of Materials Chemistry B 4 (2016).

[6] Q. Xu, Y. Liu, R. Su, L. Cai, B. Li, Y. Zhang, L. Zhang, Y. Wang, Y. Wang, N. Li, Nanoscale 8 (2016) 17919.

[7] F.F. An, J. Ye, J.F. Zhang, Y.L. Yang, C.J. Zheng, X.J. Zhang, Z. Liu, C.S. Lee, X.H. Zhang, Journal of Materials Chemistry B 1 (2013) 3144.

[8] K. Jiang, S. Sun, L. Zhang, Y. Lu, A. Wu, C. Cai, H. Lin, Angewandte Chemie 54 (2015) 5360.

[9] S.N. Baker, G.A. Baker, Angewandte Chemie 49 (2010) 6726.

[10] P. Miao, K. Han, Y. Tang, B. Wang, T. Lin, W. Cheng, Nanoscale 7 (2015) 1586.

[11] J.T. Chen, H.Q. Sun, W.L. Wang, W.M. Xu, Q. He, S. Shen, J. Qian, H.L. Gao, Acta Pharmacologica Sinica 36 (2015) 1349.

[12] S. Ruan, J. Wan, Y. Fu, K. Han, X. Li, J. Chen, Q. Zhang, S. Shen, Q. He, H. Gao, Bioconjugate Chemistry 25 (2014) 1061.

[13] J. Chen, H. Sun, S. Ruan, Y. Wang, S. Shen, W. Xu, Q. He, H. Gao, Rsc Advances 5 (2015) 38547.

[14] Z. Lei, M. Zhao, L. Dang, L. An, M. Lu, A.Y. Lo, N. Yu, S.B. Liu, Journal of Materials Chemistry 19 (2009) 5985.

[15] W. Zhou, S. Dong, Y. Lin, C. Lu, Chemical Communications 53 (2017) 2122.

[16] A. Zhu, Z. Luo, C. Ding, B. Li, S. Zhou, R. Wang, Y. Tian, The Analyst 139 (2014) 1945.

[17] J. Tang, B. Kong, H. Wu, M. Xu, Y. Wang, Y. Wang, D. Zhao, G. Zheng, Advanced Materials 25 (2013) 6569.

[18] J. Chen, X. Cun, S. Ruan, Y. Wang, Y. Zhang, Q. He, H. Gao, Rsc Advances 5 (2015) 57045.

[19] J. Qian, S. Ruan, X. Cao, X. Cun, J. Chen, S. Shen, X. Jiang, Q. He, J. Zhu, H. Gao, Journal of Colloid & Interface Science 436 (2014) 227.

[20] C. Yu, X. Li, F. Zeng, F. Zheng, S. Wu, Chemical Communications 49 (2013) 403.

[21] H. Wang, S. Mukherjee, ACS Applied Materials & Interfaces 9 (2017) 18639.

[22] C. Yu, Y. Wu, F. Zeng, S. Wu, Journal of Materials Chemistry B 1 (2013) 4152.

[23] J. Wang, C. Zhang, L. Liu, K.A. Kalesh, L. Qiu, S. Ding, M. Fu, L.Q. Gao, P. Jiang, Electrophoresis 37 (2016) 2156.

[24] V.N. Mehta, S. Jha, H. Basu, R.K. Singhal, S.K. Kailasa, Sensors & Actuators B Chemical 213 (2015) 434.

[25] W. Xiao, Y. Li, C. Hu, Y. Huang, Q. He, H. Gao, Journal of Colloid & Interface Science 497 (2017) 226.

[26] S. Ruan, J. Qian, S. Shen, J. Zhu, X. Jiang, Q. He, H. Gao, Nanoscale 6 (2014) 10040.

[27] H. Ding, S.B. Yu, J.S. Wei, H.M. Xiong, ACS Nano 10 (2016) 484.

[28] P. Zhao, Q. Xu, J. Tao, Z. Jin, Y. Pan, C. Yu, Z. Yu, Nanomedicine and Nanobiotechnology (2017).

[29] H. Maeda, J. Wu, T. Sawa, Y. Matsumura, K. Hori, Journal of Controlled Release 65 (2000) 271.

[30] K.N. Sugahara, T. Teesalu, P.P. Karmali, V.R. Kotamraju, L. Agemy, O.M. Girard, D. Hanahan, R.F. Mattrey, E. Ruoslahti, Cancer Cell 16 (2009) 510.

[31] A.K. Iyer, G. Khaled, J. Fang, H. Maeda, Drug Discovery Today 11 (2006) 812.

[32] T. Stylianopoulos, E.A. Economides, J.W. Baish, D. Fukumura, R.K. Jain, Annals of Biomedical Engineering 43 (2015) 2291.

[33] Y. Zhong, F. Meng, C. Deng, Z. Zhong, Biomacromolecules 15 (2014) 1955.

[34] R. van der Meel, L.J. Vehmeijer, R.J. Kok, G. Storm, E.V. van Gaal, Advanced Drug Delivery Reviews 65 (2013) 1284.

[35] S. Ruan, W. Xiao, C. Hu, H. Zhang, J. Rao, S. Wang, X. Wang, Q. He, ACS Applied Materials & Interfaces 9 (2017) 20348.

[36] G. Hu, X. Chun, Y. Wang, Q. He, H. Gao, Oncotarget 6 (2015) 41258.

[37] X. Tian, L. Zhang, M. Yang, L. Bai, Y. Dai, Z. Yu, Y. Pan, Nanomedicine and Nanobiotechnology (2017).

[38] M. Shadidi, M. Sioud, Drug Resistance Updates 6 (2003) 363.

[39] S. Lee, J. Xie, X. Chen, Chemical Reviews 110 (2010) 3087.

[40] W. Arap, R. Pasqualini, E. Ruoslahti, Science 279 (1998) 377.

[41] E. Ruoslahti, Nature reviews. Cancer 2 (2002) 83.

[42] J.S. Desgrosellier, D.A. Cheresh, Nature Reviews. Cancer 10 (2010) 9.

[43] T. Teesalu, K.N. Sugahara, V.R. Kotamraju, E. Ruoslahti, Proceedings of the National Academy of Sciences of the United States of America 106 (2009) 16157.

[44] H. Xie, X. Xu, J. Chen, L. Li, J. Wang, T. Fang, L. Zhou, H. Wang, S. Zheng, Chemical Communications 52 (2016) 5601.

[45] J. Wang, H. Wang, L. Jie, Z. Liu, H.Y. Xie, X. Wei, L. Di, R. Zhuang, X. Xiao, S. Zheng, ACS Applied Materials & Interfaces 8 (2016) 19228.

[46] R.K. Jain, T. Stylianopoulos, Clinical Oncology 7 (2010) 653.

[47] G. Gu, X. Gao, Q. Hu, T. Kang, Z. Liu, M. Jiang, D. Miao, Q. Song, L. Yao, Y. Tu, Z. Pang, H. Chen, X. Jiang, J. Chen, Biomaterials 34 (2013) 5138.

[48] Z. Cheng, A. Al Zaki, J.Z. Hui, V.R. Muzykantov, A. Tsourkas, Science 338 (2012) 903.

[49] N. Zhao, B. Wu, X. Hu, D. Xing, Biomaterials 141 (2017) 40.

[50] E. Doolittle, P.M. Peiris, G. Doron, A. Goldberg, S. Tucci, S. Rao, S. Shah, M. Sylvestre, P. Govender, O. Turan, Z. Lee, W.P. Schiemann, E. Karathanasis, ACS Nano 9 (2015) 8012.

[51] S. Hussain, M. Rodriguez-Fernandez, G.B. Braun, F.J. Doyle, 3rd, E. Ruoslahti, Scientific Reports 4 (2014) 5232.

[52] C.N. Landen, T.J. Kim, Y.G. Lin, W.M. Merritt, A.A. Kamat, L.Y. Han, W.A. Spannuth, A.M. Nick, N.B. Jennnings, M.S. Kinch, D. Tice, A.K. Sood, Neoplasia 10 (2008) 1259.

[53] C. Hu, Y. Liu, J. Chen, Q. He, H. Gao, Journal of Colloid & Interface Science 480 (2016) 85.

[54] H. Gao, Q. He, Expert Opinion on Drug Delivery 11 (2014) 409.

[55] L. Alberici, L. Roth, K.N. Sugahara, L. Agemy, V.R. Kotamraju, T. Teesalu, C. Bordignon, C. Traversari, G.P. Rizzardi, E. Ruoslahti, Cancer Research 73 (2013) 804.

[56] S. Ruan, C. Hu, X. Tang, X. Cun, W. Xiao, K. Shi, Q. He, H. Gao, ACS Nano 10 (2016) 10086.

[57] E. Ruoslahti, Advanced Materials 24 (2012) 3747.

[58] H.J. Cho, S.J. Lee, S.J. Park, C.H. Paik, S.M. Lee, S. Kim, Y.S. Lee, Journal of Controlled Release 237 (2016) 177.

[59] K.N. Sugahara, T. Teesalu, P.P. Karmali, V.R. Kotamraju, L. Agemy, D.R. Greenwald, E. Ruoslahti, Science 328 (2010) 1031.

*3: Graphical Abstract

Click here to download high resolution image